Stress Above Wind Plus Paddle Waves: Modelling of a Laboratory Experiment

V. K. Makin
Royal Netherlands Meteorological Institute (KNMI), De Bilt, Netherlands

H. Branger
Institut de Recherche sur les Phénomènes Hors Equilibre, CNRS, Université de Provence, Aix-Marseille Université, Marseille, France

W. L. Peirson
Water Research Laboratory, School of Civil and Environmental Engineering, The University of New South Wales, Manly Vale, Australia

J. P. Giovanangeli
Institut de Recherche sur les Phénomènes Hors Equilibre, CNRS, Université de Provence, Aix-Marseille Université, Marseille, France

March 29, 2007

Short title: STRESS ABOVE WIND PLUS PADDLE WAVES: MODELLING OF A LABORATORY EXPERIMENT

Abstract. A Wind-Over-Waves Coupling (WOWC) model is used to simulate a laboratory experiment and to explain the observed peculiarities of the surface stress distribution above a combined wave field: wind-generated plus monochromatic paddle waves. Observations show the systematic and significant decrease in the stress as the paddle wave is introduced into the pure wind-wave field. As the paddle wave steepness is further increased, the stress level returns to the stress level characteristic of the pure wind waves. Further increase in the paddle wave steepness augments the stress further. The WOWC model explains this peculiarity of the stress distribution by the fact that the paddle waves significantly damp the wind waves in the spectral peak. The stress supported by these dominant waves rapidly falls when the paddle wave is introduced, and this decrease is not compensated by the stress induced by the paddle wave. With further increase in the steepness of the paddle wave, the stress supported by dominant wind waves stays at a low level, while the stress supported by the paddle waves continues to grow proportional to the square of the steepness, finally exceeding the stress level characteristic of the pure wind wave field.

1. Introduction

One complication in the study and understanding of air-sea interactions on the open ocean is the presence of swell on the ocean surface. Mixed wind sea - swell or pure swell conditions are the most common feature of the open ocean. Yelland and Taylor (1996) found that in the open ocean at low wind speeds, the drag coefficient increases with a decrease in the wind speed. This rather rapid increase cannot be explained by the aerodynamically smooth condition of the sea surface. The authors also mention that during the ocean cruise, the wave field at low winds was always dominated by swell and that it is very likely that the impact of swell on the atmosphere could result in a strong increase in the drag coefficient at low winds. Donelan et al. (1997) found a strong increase in the drag coefficient at low winds (less than 6 ms^{-1}) in the presence of swell travelling across or opposite to the wind. No impact was detected in favorable winds. This finding was confirmed by Drennan et al. (1999). They concluded that much of the scatter in the drag coefficient could be attributed to the presence of swell. However, no quantitative relations describing the impact of swell on the sea surface drag were proposed, nor the physical mechanisms responsible for the impact were revealed. Concurrently, the directional ocean wave spectrum was measured during campaigns (Donelan et al. 1997; Drennan et al. 1999). They were used to determine the condition of the ocean surface and to separate swell from the wind sea. No detailed analysis of the interaction of swell with the wind sea was reported.

Under laboratory conditions, the mixed sea is modelled by the interaction of a mechanically generated monochromatic paddle wave with wind-generated waves. The conditions in the laboratory are better controlled and the measurements of the stress above the wave field and the wave field itself is simpler than in the ocean. Previous laboratory work (Mitsuyasu, 1966; Phillips and Banner, 1974; Hatori et al., 1981; Donelan, 1987) has shown that long paddle waves propagating in the wind direction could have a significant effect on the wind-generated wave spectrum. The energy of the wind-generated waves, which is mainly the energy of the dominant waves (waves in the spectral peak of the wind-wave spectrum), was shown to reduce by up to 20% in the presence of the paddle waves as compared to pure wind-generated waves. Unfortunately, no stress measurements were made. Simultaneous measurements of stress above wind-generated and paddle waves and waves were reported recently by Peirson et al. (2004). The authors have found that with increasing steepness of the paddle wave, the stress first drops compared to the situation of pure wind-generated waves, and then rapidly increases with further increase of the wave steepness. The result seems to totally contradict results obtained in the open ocean, where no stress changes were obtained for swell propagating in the wind direction.

Here, it is time to realize the difference between the mixed wind sea - swell in the open ocean and the wind-generated - paddle waves in the laboratory. Ocean swell is generally defined as non-locally generated waves that propagate into a region of locally generated wind waves. The swell often propagates from distant storms and is more likely to be long and smooth crested. Therefore, they are often observed as long waves separated in frequency space from wind waves. The magnitude of their phase speeds are often larger than the wind speed. However, observations indicate that the direction of the swell relative to the wind velocity vector is a key consideration for air-sea interaction. When the swell propagates in the direction of the wind it is slightly coupled to the atmosphere meaning that the energy and momentum loss is small (otherwise it could not cross the oceans and survive for days). However, the coupling increases when the swell is propagating at the angle and especially against the wind as demonstrated by the experimental results of Donelan et al. (1977) and Drennan et al. (1999), and shown theoretically by Kudrayvtsev and Makin (2004). Monochromatic waves in the laboratory are also separated in frequency space from the wind-generated waves, but because of the limited dimensions of the tanks, they cannot be made long enough to travel faster than the wind. Consequently paddle waves are always slow waves meaning that they are strongly coupled to the atmosphere, extracting a considerable part of the total energy and momentum flux from the wind. This in turn provides a strong interaction of the paddle wave with the wind waves via the atmosphere, which is most likely small in the open ocean at least for the swell propagating with the wind. This strong coupling is explained in terms of the spectral sheltering mechanism, which follows from the Wind-Over-Waves Coupling (WOWC) theory - a modern theory of microscale air-sea interaction. WOWC relates the momentum flux (or surface stress or sea drag) directly to the properties of wind waves and the peculiarities of their interaction with the wind and ocean surface phenomena, and also explains the formation of fluxes and their variability. It was developed in the last decade (Makin et al., 1995; Makin and Kudryavtsev, 1999, 2002; Kudryavtsev et al., 1999; Kudryavtsev and Makin, 2001). The growth of wind waves is defined by the local stress near the surface, which is only a part of the total stress because the steep paddle wave supports a considerable part of the total stress. This leads to the suppression of wind waves. Chen and Belcher (2000), following this idea, developed a model and showed that indeed the suppression of wind waves by the paddle wave in the laboratory conditions could be explained by the spectral sheltering mechanism. The effect becomes more pronounced with increasing paddle wave steepness. Swell moving with the wind in the ocean does not support the total stress. To the contrary, the momentum flux is directed from swell to the atmosphere, which reduces the total stress. The spectral sheltering mechanism in the mixed wind waves plus swell field does not exist in the ocean for the swell travelling in the wind direction, and neither does the suppression of wind waves (due to this mechanism). To conclude, it is not appropriate to refer to the paddle waves moving with the wind in the laboratory as to "swell", because the physical mechanisms of the interaction of swell with the atmosphere and wind waves is different from the interaction of the paddle waves with the wind and wind-generated waves in the laboratory.

The WOWC theory was successfully applied to open ocean (pure wind sea waves)

(Kudryavtsev and Makin, 2001), developing wind seas (Makin and Kudryavtsev, 2002; Guo-Larsen et al., 2003), and in the rather small George Lake in Australia (Babanin and Makin, personal communication) to explain the observed behaviour of the sea drag. It explains the wind speed, wave age and finite depth dependencies of the sea drag (drag coefficient), and gives reasonable qualitative agreement with measurements. The WOWC theory provides an excellent tool for data interpretation. The main objectives of the present study are to apply the theory to the wave field in the laboratory conditions and to make an interpretation of the stress measurements above a combined wave field that consists of pure wind-generated waves and monochromatic paddle waves.

Here, we report a simulation of a laboratory experiment performed in the European Large Air-Sea Interaction Facility of the Institute de Recherche des Phénomènes Hors Equilibre (IRPHE) by means of the WOWC model. The WOWC model contains quite a number of empirical parameters. The choice of these parameters is discussed in detail in the previous papers referenced above. The general usefulness of the WOWC model depends on how well it performs using fixed values for free parameters - i.e., that they can be considered "empirical constants". To this end, the model with the parameters fixed in the previous studies is applied here to explain the observed peculiarities of the surface stress distribution in the laboratory. This is the methodology of the present approach. It appears that the WOWC model reproduces well the stress measurements above this complex wave field. The model explains the observed peculiarity of the stress distribution by the peculiarity of the interaction of the paddle waves with the wind wave field, and by the peculiarity of the stress balance above wind-generated plus paddle wave field. The precise description the laboratory experiment and the WOWC model is given in Sections 2 and 3; the results of the numerical simulation are described in Section 4. Concise conclusions are presented at the end of the paper.

2. Experiment

The experiment was performed in the Institute de Recherche des Phénomènes Hors Equilibre tank of the CNRS-Université de la Méditerranée in Marseille, France (Peirson et al., 2004). This is a large wind-wave facility consisting of a recirculating air tunnel 40 m long with a 1.6 m high air cavity overlying a water tank 2.6 m wide and 1 m deep. A submerged wavemaker at the upwind end was used to generate long monochromatic water waves propagating in the wind direction with frequencies between 1.4 and 2.0 Hz. The upwind end of the tank is specially profiled to ensure minimum disturbance to either the generation of mechanical waves or the turbulent boundary layer in the air flow above the waves. A fan in the air recirculation cavity was used to generate winds between 6 and 10 ms^{-1} in the test section. The tunnel roof is careful profiled to create an air flow boundary layer with constant momentum flux adjacent to the water surface along the test section of the tank. At the downwind end of the tank a permeable absorbing beach was installed to minimize wave reflection. A complete description of the tank can be found in Coantic et al. (1981).

At short fetch, the total stress in the air immediately above the water surface increases rapidly with fetch due to wave drag created by the developing wind-generated wave field (e.g. Banner and Peirson, 1998). Previous testing in the IRPHE tank had shown that approximately 9 m from the inlet, the drag saturates and shows no further increase along the tank. To avoid possible stress fetch dependence, measurements were performed at a fetch of 21 m. It should be mentioned that steep wave trains could be unstable in a number of modes that develop with fetch (Kharif and Ramamonjiarisoa, 1988), so that some observations were vulnerable to instabilities in the wave field.

Small X-probe constant temperature anemometers (CTAs) were used to measure the total stress applied to the water surface. Each probe was amplified and digitized at a rate of 300 Hz in blocks of 5 minutes. For each block, the mean velocity was computed and the residual fluctuating velocity components were used to calculate the mean turbulent stress. A Pitot tube was used to monitor any drift in the hot wires during their operation.

Prior to testing, it was confirmed that a constant stress layer existed within 0.10 m of the mean water surface at the highest test wind speed thereby ensuring that stress measurements obtained within 0.10 m of the surface will be reliable. The measurements of total stress above steep, long monochromatic waves at a wind speed of 10 ms^{-1} required that the CTAs be raised to 0.13 m above the mean water surface. The stress profiles indicated that at this elevation, the measured values will not underestimate the total stress by more than 10%.

The wave field was measured by two capacitance wave probes spaced at 0.050 m and aligned along the axis of the tank. Each probe was digitized at a rate of 300 Hz, and the data were stored for subsequent processing.

It was also important to obtain the steepness of the monochromatic low frequency waves at the observation point. This was accomplished by: filtering wave energy at frequencies greater than $3f_m$ from the record (where f_m is the frequency of the monochromatic paddle wave); extracting individual waves from the filtered record by up crossing analysis; and, evaluating the mean steepness AK as half of the mean wave height of all waves A multiplied by the equivalent linear wave number of the long waves K. It should be noted that the term 'long wave ' is used here to indicate that the monochromatic waves generated in the experiment were longer than the waves in the peak of the spectra of pure wind-generated waves. However, they are characterized by a large value of inverse wave age U_{10}/C (U_{10} is the wind speed extrapolated to the height of 10 m, and C is their phase velocity) typically being between 7 and 12, so that they are strongly forced/coupled to the wind. This is contrary to the situation in the ocean where long waves separated in frequency space from the wind waves and propagating in the wind direction are associated with swell. The latter are characterized by the inverse wave age parameter $U_{10}/C \leq 1$, and are weakly coupled to the wind.

The experiment consisted of several realizations during which a long wave frequency f_m and a reference wind speed in the tunnel U_{ref} were fixed and the steepness of the long waves AK was progressively increased from zero to the maximum achievable within the facility. Normally, two runs (labelled A and B) were made for the same external forcing to have an idea of internal variability of measured stress and wave parameters. For the present study four such realizations labelled G-, H-, I- and C-series were chosen. They differ in the reference wind speed and the frequency of the paddle waves.

The experimental conditions are summarized in Table 1-4 of the Appendix (the model results that enter the table will be explained later).

It should be mentioned that breaking waves were only observed visually, and only those corresponding to the paddle wave frequency were quantified. The visual evidence showed that for pure wind-generated waves and the wind speed 6 and 8 ms^{-1} (correspondingly the wave length in the peak of the spectrum was 0.22 m and 0.28 m) there were no air entraining (large-scale) breaking waves (breaking that generates foam). But steep wind waves emitting parasitic capillaries waves in the front of the waves were observed everywhere, which indicate that microscale breaking, i.e. breaking without air entrainment, is a general feature in the laboratory. At 10 ms^{-1} (where the wave length in the peak is 0.33 m) breaking was observed occasionally with thin visible whitecap and air entrainment. When the paddle waves were added, breaking becomes active when the steepness of the paddle wave AK exceeds 0.14 - 0.20. The percentage of the long wave breaking with larger-scale breakers was quantified reaching 30%, 55% and 90% correspondingly for the wind speed 6, 8 and 10 ms^{-1}.

3. The WOWC model

The detailed description of the model could be found in (Makin and Kudryavtsev 1999, 2002; Kudryavtsev et al., 1999; Kudryavtsev and Makin, 2001). Here, the precise description is given.

The WOWC approach is based on the conservation equation for integral momentum:

$$u_*^2 = \tau^\nu + \overline{p\frac{\partial \eta}{\partial x}}, \tag{1}$$

where u_* is the friction velocity, τ^ν is the viscous surface stress and $\tau^f = \overline{p\partial\eta/\partial x}$ is the form drag of the water surface, and the stresses are normalized on the density of the air ρ_a. Equation (1) reflects a fundamental fact that the stress $\tau = u_*^2$ at the surface is formed by the viscous stress and the form drag. The form drag of the water surface is a correlation of the wave-induced surface pressure field with the wave slope. The second term on the right-hand side of equation (1) is dominant for all, except very low, wind speeds. Thus the wave field and its peculiarities explain the formation of stress and its variation.

Equation (1) assumes stationary and spatial homogeneous conditions. The water surface is described statistically in terms of the directional wave variance spectrum $F(\mathbf{k})$,where $\mathbf{k}$ is the wavenumber vector. The wind direction coincides with the mean direction of wave propagation and the wave spectrum is symmetrical relative to that direction. Relating the form drag in (1) to geometrical properties of the surface (described in terms of the wave spectrum) and to the properties of the energy exchange between waves and wind, the stress at the surface is related or coupled directly to the sea state.

3.1. The form drag

Two main mechanisms of wind-wave interaction that support the form drag are distinguished. When the wavy surface is regular (in a sense that there are no wave breaking events) the wind flows over the wave smoothly, i.e. the surface is streamlined. This regime of wind-wave interaction is described in terms of the non-separated sheltering mechanism (e.g., Belcher and Hunt, 1993), which provides the energy flux to waves from the wind. This non-separated sheltering mechanism also accounts for the stress supported by microscale breaking waves. The part of the form drag supported by the non-separated sheltering mechanism, the wave-induced stress τ_w^f, can be written

$$\tau_w^f = \int_k \int_\theta \beta(k,\theta) c^2 B(k,\theta) \cos\theta d \ln k d\theta, \tag{2}$$

where $B = k^4 F$ is the saturation wave spectrum, c is the phase speed, θ is the angle, and β is the dimensionless energy flux to waves or the growth rate parameter defined as

$$\beta = \frac{1}{\omega E_k} \frac{\partial E_k}{\partial t}. \tag{3}$$

In (3) E_k is the wave energy, and $\partial E_k / \partial t = -\overline{p_k \partial \eta_k / \partial t}$ is the energy flux to a spectral wave component k with the frequency ω. The growth rate parameter is taken in the form suggested by Stewart (1974), and the angular distribution proportional to $\cos^2\theta$ as discussed by Meirink et al. (2003)

$$\beta = c_\beta \frac{u_*}{c} (\frac{u_{\lambda/2}}{c} - 1) \cos^2\theta, \tag{4}$$

where $u_{\lambda/2}$ is the wind speed at the height equals the half of the wave length λ, and $c_\beta = 1.5$ is a constant. Assuming that the wind profile is described by the logarithmic distribution (which is the case in the present experimental study)

$$U(z) = \frac{u_*}{\kappa} \ln \frac{z}{z_0}, \tag{5}$$

where z_0 is the roughness length and κ=0.41 is the Von Karman constant, the relation (4) can be rewritten in the form

$$\beta = C_\beta \left(\frac{u_*}{c}\right)^2 \cos^2\theta, \tag{6}$$

where the proportionality coefficient is dependent on wave parameters

$$C_\beta = c_\beta (\kappa^{-1} \ln \frac{\pi}{k z_0} - \frac{c}{u_*}). \tag{7}$$

With increasing wind, the waves start to visibly break on the sea surface. A significant augmentation of the surface local stress above large-scale breaking waves is reported in laboratory experiments (e.g. Banner, 1990). In these studies, it has been established that the air flow separation (AFS) from the crest of breaking waves is responsible for this augmentation. The impact of the air flow separation from breaking waves on the sea drag was accounted for in Kudryavtsev and Makin (2001). Assuming that the sea surface can be presented as a streamlined surface covered by areas, where the air flow separation takes place, and relating the stress to the wave breaking statistics, they derived a general expression for the stress supported by AFS

$$\tau_s^f = \varepsilon_b \gamma \int_{\mathbf{c}} u_s^2 \cos\theta k^{-1} \Lambda(\mathbf{c}) d\mathbf{c}. \tag{8}$$

In (8) the distribution $\Lambda(\mathbf{c})$ represents the wave breaking statistics in terms of the surface density of the total length of wave breaking fronts that have velocities in the range $\mathbf{c}$ to $\mathbf{c} + d\mathbf{c}$ (Phillips, 1985). The reference wind speed u_s is defined as the positive difference between the mean wind speed at the reference level $z_b = 1/k$ and the phase speed of the wave

$$u_s = \max(0, \frac{u_*}{\kappa} \cos\theta \ln \frac{1}{kz_0} - c). \tag{9}$$

Empirical constants entering (8) are: γ =1 and ε_b = 0.5, the latter being the characteristic slope of the breaking wave. The choice of these constants is discussed by Kudryavtsev and Makin (2001).

3.1.1. Stress supported by the AFS from equilibrium range of short gravity waves. The expression for the separation stress supported by short gravity waves in the equilibrium range of the spectrum $\tau_{s_{eq}}^f$ was obtained by Kudryavtsev and Makin (2001). Following the approach by Phillips (1985) the distribution function $\Lambda(\mathbf{c})$ was directly related to the average rate of the energy dissipation per unit area by breakers with velocities between $\mathbf{c}$ and $\mathbf{c} + d\mathbf{c}$. It was further assumed that under steady conditions the energy dissipation due to wave breaking is equal or proportional to the energy input from the wind in the equilibrium range of the wind wave spectrum. It was then shown that the total length of wave breaking fronts can be expressed in terms of the saturation spectrum as

$$\Lambda(\mathbf{c}) = \frac{\beta}{b} B(\mathbf{c}) k^{-1} \tag{10}$$

with $b = 0.01$ being an empirical constant. With (10) the relation (8) for the separation stress can be written as

$$\tau^f_{s_{eq}} = \varepsilon_b \gamma b^{-1} \int_\theta \int_{k<k_b} u_s^2 \beta(k,\theta) B(k,\theta) \cos\theta d\theta d\ln k. \tag{11}$$

The integration over the wavenumber k in (11) is performed in the wavenumber range satisfying the condition $k < k_b$, where $k_b = 2\pi/\lambda_b$ rad m^{-1} is the breaking wavenumber limit. Equation (11) describes the separation stress due to large-scale breaking characterized by air entrainment and manifesting itself in foam formation. This kind of breaking is characterized by the slope discontinuity of the breaking fronts, as discussed in Kudryavtsev and Makin (2001). Waves in $k > k_b$ domain break in a microscale sense, i.e. without air entrainment, and the loss of their energy is mainly due to the generation of the parasitic capillaries, as discussed by Kudrayvtsev et al. (1999). Though these waves are rather sharp, they could not be characterized by the slope discontinuity, and the stress they support is described in terms of non-sheltering mechanism according to (2). As parasitic capillaries are explicitly described by the model they also support the stress according to (2). These two terms parameterize the stress supported by microscale breaking. The wavelength λ_b is of O(0.1 m) as discussed by Kudryavtsev and Makin (2001). Here, the value 0.3 m is taken based on visual evidence of the present experiment and similar experiments performed in the same laboratory (photo's taken in the laboratory), and previously reported studies (Banner and Peirson, 1998; Yermakov et al., 1986).

3.1.2. Stress supported by the AFS from dominant wind waves. Dominant wind waves are the wave components at the spectral peak of the wind wave spectrum defined as $0.5k_p \leq k \leq 1.7k_p$, where k_p is the spectral peak wavenumber. For young seas and in the laboratory conditions the dominant waves can break (Babanin et al., 2001; Xu et al., 1986) and thus contribute to the separation stress and impact the sea drag. It is necessary to chose a parameterization different from (10) for the breaking wave statistics $\Lambda(\mathbf{c})$ because the assumption that dissipation is balanced by wind input is not valid in the range of the spectral peak. The statistics of dominant wave breaking will be described by a breaking wave model based on a concept of a threshold level (Longuet-Higgins, 1957; Srokosz, 1986), where it is assumed that the wave breaking event takes place when the sea surface exceeds some threshold level. It follows that

$$\Lambda(\mathbf{c})d\mathbf{c} = \frac{1}{2\pi}kP, \tag{12}$$

where P describes the breaking probability of dominant waves

$$P = \exp\left(-\frac{\varepsilon_T^2}{\varepsilon_d^2}\right), \tag{13}$$

$\varepsilon_d = H_d k_p/2$ is the dominant wave steepness, H_d is the significant wave height for dominant waves, and ε_T is a threshold steepness being a tuning constant. This is the only parameter in the model that cannot be considered as an "empirical constant" and has to be retuned. For the open ocean and long non-dimensional fetch ($X = xg/U_{10} \sim 10^5$, x being the physical fetch) the characteristic dominant wave steepness is of about 0.1. For limited fetch it increases to about 0.15 at $X = 10^3$ and 0.20 at $X = 10^2$ (Kahma and Calkoen, 1992). In the model, the breaking limit was estimated to be about 0.24 on the basis of the wave breaking probability observations of Banner et al. (2000) and Babanin et al. (2001), and this value was used through the simulations in the open ocean and seas. The dominant waves in the laboratory conditions are much steeper than in the open sea reaching values up to 0.30. It simply means that their breaking starts much later in terms of the breaking steepness limit (in statistical sense). This in turn means that the estimated breaking limit value for the open sea is not a universal parameter. Support for this statement comes from a theoretical study by Song and Banner (2002) where they argue that steepness is not an "universal" threshold parameter for the wave breaking and that this parameter depends on the wave group width. They also estimated that for a narrow wave group the threshold parameter is higher than for broader groups. As a consequence, it looks appropriate for the present modelling approach to re-estimate the breaking limit. It is taken here as 0.62. This value is based on visual quantification of the breaking probability of dominant waves obtained in the similar study performed in the same laboratory and under the same external condition (Caulliez, personal communication).

With (12) the expression for the separation stress (8) supported by dominant waves is (Makin and Kudryavtsev, 2002)

$$\tau^f_{s_d} = \frac{\varepsilon_b \gamma}{2\pi} u^2_{sd} P. \tag{14}$$

Here the reference wind speed for dominant waves u_{sd}

$$u_{sd} = \max(0, \frac{u_*}{\kappa} \ln \frac{\varepsilon_b}{k_p z_0} - c_p) \tag{15}$$

is positive and specified at the level just above the breaking dominant waves, i.e. at $z_b = \varepsilon_b / k_p$, and c_p is phase speed at the spectral peak.

3.1.3. Stress supported by the monochromatic wave. The form drag supported by the monochromatic wave can be written as

$$\tau^f_{w_m} = \frac{1}{2}(AK)^2 C_\beta(K) u^2_*, \tag{16}$$

where A is the amplitude of the monochromatic wave, K its wavenumber and $C_\beta(K)$ is calculated according to (7) at $k = K$. Equation (16) follows from the general definition of the growth rate parameter (3), where for the monochromatic wave $E = \rho_w g A^2/2$, and its form (6), where for the monochromatic wave $\theta = 0^O$. Equation (16) could be also directly obtained from a general definition of the form drag (2) keeping in mind that

$Bdk \sim Edk \sim A^2/2$.

In the experiment it was observed that the paddle waves start breaking when their mean steepness exceeds 0.2 (Peirson et al., 2004). It means that the separation of the air flow from these steep waves does occur and the separation stress cannot be neglected. However, to keep the uniform description of the form drag supported by the paddle wave in all range of the steepness we still use (16), which follows from the non-separated sheltering mechanism. The possibility to do so is justified by the study by Maat and Makin (1992). They simulated a laboratory experiment by Banner (1990), who measured the pressure distribution above breaking, steep, monochromatic waves. It appeared that the distribution of pressure (and thus the momentum and energy flux) above breaking monochromatic waves could be well described in terms of non-separated sheltering mechanism (their Figure 1) being applied to steep monochromatic waves of finite amplitude.

3.2. Viscous stress

Patching the linear wind profile inside the viscous layer with the logarithmic wind profile above it, the viscous stress can be written

$$\tau^{\nu} = (\kappa d)^{-1} \frac{\delta}{z_0} u_*^2, \tag{17}$$

where

$$\delta = d \frac{\nu}{u_*} \tag{18}$$

is the thickness of the viscous sublayer, ν is the molecular viscosity, $d = 20$ is a constant, and z_0 is the roughness parameter defined through the logarithmic wind profile (5) extending to the surface from a height where the wind velocity is not influenced by the wave motions.

3.3. Resistance law of the sea surface

Equation (1), where viscous stress is calculated according to (17) and the form drag τ^f can be evaluated through (2), (11), (14), and (16)

$$u_*^2 = \tau^\nu + \tau_w^f + \tau_{s_{eq}}^f + \tau_{s_d}^f + \tau_{w_m}^f \tag{19}$$

describes the resistance law of the sea surface that relates the stress to the properties of the wave field. Given the wind speed at a specified height and a wave spectrum, Equation (19) is solved by iterations to provide the surface stress (friction velocity). It should be stressed here that the friction velocity follows from a solution of the model. When the solution for u_* is obtained it could be presented in terms of the roughness parameter z_0, which is uniquely related to the friction velocity through (5) where U_{10} is given as an input to the model.

Finally, it is worthwhile to mention that the ultimate goal of an experiment would be to measure separately all terms of the stress in equation (19) and to compare those with the model results. Unfortunately that is technically impossible at present. However, a good comparison of model calculations of the total stress with data obtained in the previous and, as will be seen, in the present study provides confidence that the stresses in (19) are treated in the right way and the model is robust.

3.4. Specification of the wave spectrum

To obtain the stress as a function of the wind speed and wave age an empirical wave spectrum or a physical model of the wave spectrum is required. To calculate the stress due to the AFS supported by short gravity waves $\tau_{s_{eq}}^f$, the equilibrium part of the wave spectrum defined at $1.7k_p < k < k_b$ has to be known. The calculation of the separation stress supported by dominant wind waves $\tau_{s_d}^f$ requires the shape of the spectrum at the spectral peak, while the calculation of the wave-induced stress τ_w^f requires the shape of the spectrum in the wavenumber range from capillary waves to the spectral peak

$B(k, \theta)$. The spectrum B is split into two parts: the low B_l and the high wavenumber spectrum B_h

$$B(k, \theta) = B_l(k, \theta) + B_h(k, \theta). \tag{20}$$

In the tank, with the wave gauges, only the frequency spectra were measured and not the wavenumber spectra. The measured high frequency spectrum cannot be uniquely converted to the wavenumber spectrum because the former is vulnerable to the Doppler effects and the dispersion relation is not known. Consequently, a physical model of the short wave spectrum is required. Such model was developed by Kudryavtsev et al. (1999). The model is based on the energy balance equation and accounts for wind input, viscous dissipation, dissipation due to wave breaking, including large-scale and microscale breaking, and nonlinear three-wave interaction. The details of the model and its verification in terms of some integral and spectral wave parameters against a number of experiments can be found in Kudryavtsev et al. (1999).

The shape of the low wavenumber (at the spectral peak) spectrum B_l is given by the empirical model by Donelan et al. (1985). The spectral shape of B_l is defined by the inverse wave age parameter U_{10}/c_p, where U_{10} is a measured wind speed taken from the Tables, and c_p is the phase speed at the spectral peak calculated from the measured peak frequency f_p (see the Tables) using dispersion relation $c = g/(2\pi f)$.

For the low wavenumber spectrum B_l a measured frequency spectrum converted to the wavenumber spectrum spectrum and with an empirical angular function (for example, Elfouhaily et al., 1997) as a model input could be used. In fact, few experiments supplying the model with a measured spectrum as described above were made. It was found out that the stress using the measured spectra never exceeded 10% of the stresses using the empirical spectra. That is explained by the fact that most of the stress is supported by the short waves through different mechanisms (Makin and Kudryavtsev, 2003), so that the detailed form of the low wavenumber spectrum is not important for the present study. The only important thing is that the damping of dominant waves is described correctly, as will be shown in Figure 2. So, we proceeded with the study by using the spectral model by Donelan et al. (1985).

For a given wind speed the model provides the sea surface stress, which is a function of the saturation spectrum B. The saturation equilibrium spectrum B_h in turn depends on the momentum flux, which is defined by the sea stress. Thus the wind waves and the atmospheric boundary layer are coupled, thereby forming a self-consistent dynamic system.

4. Modelling of the experiment

The main experimental result concerning the peculiarities of the stress distribution above combined wave field represented by pure wind-generated waves plus paddle monochromatic waves was originally obtained by Peirson et al. (2004) and is depicted in Figure 1. Here the ratio τ_{pww}/τ_{ww} of the total stress supported by wind-generated and paddle waves τ_{pww} to the stress supported by the wind-generated waves in the absence of paddle waves τ_{ww} (the latter is taken as the mean between A and B runs) is shown as a function of the monochromatic wave steepness AK. The data collapse approximately on one curve. In the simple normalization selected here, the development of normalized stress with increasing AK is indistinguishable between the experiment series at the degree of precision permitted by the measurements. The systematic and significant decrease in the stress is observed as paddle waves were introduced at low frequency. A minimum is achieved at about $AK = 0.14$, which is about 80% of τ_{ww}. The stress level returns to τ_{ww} at about $AK = 0.22$. With further increase in the steepness AK the stress τ_{pww} rapidly increases reaching values of about 170-180% of τ_{ww} at maximum observed steepness of the paddle wave.

It is well established that paddle waves significantly damp the dominant wind waves (Mitsuyasu, 1966; Phillips and Banner, 1974; Hatori et al., 1981; Donelan, 1987). A typical example is shown in Figure 2. One possible mechanism of this damping is explained in the Introduction as a result of the spectral sheltering (Chen and Belcher, 2000). However, we shall not speculate here on physical mechanisms that lead to this damping and do not include the spectral sheltering mechanism in the present model. Our goal here is to explain the distribution of stress above the complex wave field. So, we rather take the damping of dominant waves as an empirical fact and include it in the model as described below.

The damping of the dominant wind waves can be quantified by a damping parameter γ_d defined as

$$\gamma_d = \frac{\int F_{pww}(f)df}{\int F_{ww}(f)df}, \tag{21}$$

where $F_{pww}(f)$ is a wave spectrum for the composite wave field (paddle wave plus wind-generated waves), $F_{ww}(f)$ is a spectrum for wind waves alone, and the integration is done in the frequency range $0.7f_p \leq f \leq 1.3f_p$, $(0.5k_p \leq k \leq 1.7k_p)$, with f_p being the peak frequency of the dominant wind-generated waves. A small upshift of the wind-generated wave peak frequency observed in the presence of a paddle wave did not exceed 7% of f_p and was neglected. As already discussed, steep paddle waves could develop unstable side band harmonics, which could coalesce with the dominant wind waves. To separate the dominant wind waves from those harmonics and to estimate γ_d, we simply cut them off. This of course makes the estimate of the damping parameter less accurate. The procedure was applied to all measured spectra and the estimated values of the damping parameter are shown in the Tables and Figure 3. Again the damping parameter collapses approximately on one curve. It falls rapidly to the level of about 0.18±0.08 with the steepness AK increasing from zero to 0.14, and then remains at approximately constant level with further increase in the steepness beyond $AK = 0.14$. This is in agreement with findings by Mitsuyasu (1966), Phillips and Banner (1974), Hatori et al. (1981) and Donelan (1987). From the comparison of the stress distribution in Figure 1 with the distribution of the damping parameter it is clear that the stress ratio should be related to the damping of the dominant wind waves.

Here we interpret the observed peculiarities of the stress above combined wind-generated waves plus the paddle wave field using the WOWC model. The WOWC model is forced by the observed (calculated from the observations) wind speed at the height of 10 m, U_{10}. For the pure wind-generated waves condition, the model is supplied with the measured frequency in the peak of the wind wave spectrum f_p (taken as the mean between A and B runs). The phase speed velocity at the spectral peak c_p is calculated according to $c_p = g/2\pi f_p$. U_{10} and c_p define the inverse wave age parameter U_{10}/c_p, which is used to reconstruct the modelled low frequency wave spectrum $B_l(k,\theta)$ in the absence of paddle waves. The stress is then calculated from (19). For the combined wave field the observed steepness AK and the wavenumber $K = (2\pi f_m)^2/g$ defines the stress supported by the paddle monochromatic wave (16). The damping of the dominant wind waves is introduced through the damping of the modelled low frequency spectrum by simply multiplying it by the damping parameter in the corresponding wavenumber range according to

$$B_l(k,\theta)_{pww} = \gamma_d B_l(k,\theta). \tag{22}$$

The damped spectrum (22) is then used in (20) instead of $B_l(k,\theta)$. The model spectrum (22) for the pure wind-generated waves and the wind-generated waves spectrum damped by the paddle wave is compared with the measured spectra in Figure 2. In both cases the model spectra reproduce quite well the density of the spectral peak, but somewhat narrower in the frequency space. However, for the crude approach taken here to model the damping of the wind wave spectrum by the paddle wave by assuming the constant damping factor γ_d, the agreement is reasonable. The main feature - the damping of the spectral peak - is captured by the model. Experimental series G, H, I and C were modelled with the measured parameters listed in the Tables.

Model results for the stress (friction velocity) are listed in the Tables and are shown in Figure 4 in the form of a scatter plot. The comparison is satisfactory, the model results are within the accepted experimental overall error of 20% for the stress measurements. The slope of the regression line is 1.05, the intercept is -0.004 and the correlation coefficient is 0.99. The ratio τ_{pww}/τ_{ww} for the modelled stress is shown in Figure 5. The model results remarkably follow the measured ones. The systematic and significant decrease in the stress is well modelled as paddle waves were introduced at low frequency. A minimum is achieved in the same range of the steepness of about $AK = 0.14$, and its level is about 80% of τ_{ww}. The stress level returns to τ_{ww} at the same as observed value of AK being about 0.20. The modelled stress τ_{pww} shows the same as observed tendency of rapid increase with further increase of the steepness. It reaches the value of about 180-200% of τ_{ww}, which is somewhat higher than the observed value. It should be noted that for the I-series the modelled stress ratio is somewhat higher than the modelled ratio for the rest of the series. It is noticed that for the same external forcing applied to I- and C-series (pure wind wave conditions) the wind speed for the I-series is systematically lower that for the C-series (see Tables 3 and 4). The model being forced by this wind produces lower values of the stress, and as a consequence higher values of the stress ratio.

The peculiarity of the stress distribution could be explained from the analysis of the stress balance in (19). The main components of the balance are shown in Figure 6 for G-series and H-series. The wave-induced stress due to non-separated sheltering mechanism τ_w^f, equation (2), is additionally split into the part supported by dominant wind-generated waves in the range $0.5k_p \leq k \leq 1.7k_p$, $\tau_{w_d}^f$, and the part supported by waves in the equilibrium range $1.7k_p < k$, $\tau_{w_{eq}}^f$. Notice, that the total stress shown in the Figure $\tau_{tot} = u_*^2$. It is first noted that wind-generated waves in the laboratory conditions are very narrow in the k-range. The wavelength in the peak of the spectra $\lambda_p = 2\pi/k_p$ is 0.32 m and 0.27 m for G- and H-series, and 0.23 m, for I- and C-series correspondingly. As specified by equation (11) separation can take place for the wave components longer than λ_m >0.3 m, as shorter waves generate parasitic capillaries rather than break, and do not support the separation stress. It means that under conditions specified by the present study the separation stress is negligible, and is not shown in the Figure. For the pure wind-generated waves the wave-induced stress supported by dominant waves $\tau^f_{w_d}$ contributes most to the total stress. Smaller but comparable amounts are contributed by the wave-induced stress from the equilibrium range $\tau^f_{w_{eq}}$, and by viscous stress τ^γ. When the low steepness paddle waves are introduced, the dominant wind waves are damped and the stress supported by them rapidly falls. The minimum is achieved at the steepness of about $AK = 0.14$. The stress due to equilibrium range and the viscous stress remain roughly on the same level in this range of the paddle wave steepness. The stress supported by the paddle wave increases but slower than the decrease of the stress supported by the dominant wind-generated waves. This explains the decrease in the total stress in the range of the paddle wave steepness of $0 < AK < 0.14$. For a steepness higher than 0.14 $\tau^f_{w_d}$ remains roughly on the same level, $\tau^f_{w_{eq}}$ is decreasing with increasing steepness, and the viscous stress is quenched. The total decrease of these three parts of the total stress cannot compensate the steep increase of the stress supported by the paddle wave, which is proportional to $(AK)^2$, and the total stress rapidly increases.

The fractional contribution of the stress components in (19) to the total stress for three typical situations: pure wind-generated waves, wind-generated plus paddle waves for the paddle wave steepness less than 0.14, and wind-generated plus paddle waves for $AK > 0.14$ is shown in Figure 7. The stresses are normalized by the total stress u_*^2, so that τ_{tot} equals 100%. The distribution changes substantially across the range of AK investigated. For the pure wind-generated waves, $\tau^f_{w_d}$ contribute about 45% of the total, $\tau^f_{w_{eq}}$ contributes about 40% and the viscous stress - about 15%. When the paddle wave is just introduced, the contribution of $\tau^f_{w_d}$ drops to about 15%, $\tau^f_{w_{eq}}$ and τ^γ remain approximately on the same level, and the paddle wave contributes about 29%. For steep paddle waves, this contribution increases to 70%, and the rest of the stress is supported by the wave-induced stress.

The overshoot of the modelled stress over the observed stress for the steepest paddle waves could be explained by the spectral sheltering mechanism discovered by Makin and Kudryavtsev (1999). The growth of the shortest wind waves is defined by the local stress near the surface, which is only a part of the total stress because the steep paddle wave and dominant wind-generated waves supports a considerable part of the total stress: $\tau^l = \tau_{tot} - \tau^f_{w_m} - \tau^f_{w_d}$. This value of τ^l should be used in (6) instead of the total stress u_*^2. This would lead to the suppression of these shortest waves and correspondingly of the stress they support, and to some reduction of the total stress. In the present version of the WOWC model this sheltering effect is not accounted for explicitly. However, for the present study that is not crucial as the results of the comparison with observations and conclusions will not change, and the effect could be of marginal significance only for the steepest paddle waves.

5. Conclusions

The WOWC model is able to reproduce the stress measurements in the laboratory environment above a complex wave field consisting of the wind-generated waves and superposed paddle monochromatic waves. The modelled stress differs from that observed by not more than 20%, an acceptable error level for these stress measurements.

Peculiarities of the observed stress distribution are explained by peculiarities of the interaction of paddle waves with wind-generated waves in the laboratory conditions, and peculiarities in the stress balance. The paddle wave suppresses the dominant wind-generated waves and their associated wind-induced stress. The paddle waves support their own stress contribution, which is proportional to their steepness squared. When the steepness of the paddle wave is small the reduction in the wave-induced stress to the dominant wind-generated waves is not compensated by the paddle stress, so that the total stress is less than that above pure wind-generated waves. With increasing steepness, the stress supported by the dominant wind-generated waves levels off at the reduced value, while the stress supported by the paddle wave continues to grow. The result is that with increasing the paddle wave steepness the total stress returns to the level observed above pure wind-generated waves and then overshoots this level increasing approximately to twice the value of the original stress above pure wind-generated waves.

For the laboratory conditions studied here, the stress supported by the airflow separation from the wind-generated waves plays only a marginal role in the stress balance. The model explains this by the fact that the wave spectra are very narrow in the wavenumber range and their peak wavenumber is close to the threshold value for the breaking waves. Under these conditions, steep wind-generated waves generate parasitic capillary waves rather than break.

The non-separated sheltering mechanism plays the central role here. The dominant wind-generated waves support half of the stress because they are strongly coupled to the airflow. The 'long' paddle waves are also strongly coupled to the wind. That explains the peculiarities in the stress distribution in the laboratory conditions above the composite wave field: wind-generated plus paddle waves. In the ocean, long waves, separated in frequency space with the wind-generated waves, are usually associated with swell. These swell waves can be weakly to strongly coupled to the atmosphere depending on their propagation direction relative to the wind. However, swell propagating with the wind is weakly coupled to the atmosphere, so that the effect of long waves on the stress observed in the laboratory conditions is not expected to happen in the ocean.

The results of the present study once again show that the interpretation of field data by using results obtained in the laboratory conditions should be done with great care. On the other hand the WOWC model, which describes equally well the stress above ocean waves and in the laboratory conditions could serve as a reliable tool/link for such kind of interpretations.

Acknowledgments

The authors would like to thank Mr. Bertrand Zucchini and Alain Laurence for their helpful technical assistance during the experimental investigation.

Appendix

Tables

References

Babanin, A.V., I.R. Young, and M.L. Banner, 2001: Breaking probability for dominant waves on water of finite constant depth. *J. Geophys. Res.*, **106**, 11659-11676.

Banner, M.L., 1990: The influence of wave breaking on the surface pressure distribution in wind wave interaction. *J. Fluid Mech.*, **211**, 463-495.

Banner, M.L., and W.L. Peirson, 1998: Tangential stress beneath wind-driven air-water interfaces. *J. Fluid Mech.*, **364**, 115-145.

Banner, M.L., A.V. Babanin, and I.R. Young, 2000: Breaking probability for dominant waves on the sea surface. *J. Phys. Oceanogr.,* **30,** 3145-3160.

Belcher, S.E., and J.C.R. Hunt, 1993: Turbulent shear flow over slowly moving waves. *J. Fluid Mech.*, **251**, 109-148.

Chen, G., and S.E. Belcher, 2000: Effects of long waves on wind-generated waves. *J. Phys. Oceanogr.,* **30,** 2246-2256.

Coantic, M., A. Ramamonjiarisoa, P. Mestayer, F. Resch, and A. Favre, 1981: Wind water tunnel simulation of small-scale ocean-atmosphere interactions. *J. Geophys. Res.*, **86**, C7, 6607-6626.

Donelan, M.A., 1987: The effect of swell on the growth of wind waves. *Johns Hopkins APL Tech. Dig.*, **8**, 18-23.

Donelan, M.A., W.M. Drennan, and K.B. Katsaros, 1997: The air-sea momentum flux in conditions of wind sea and swell. *J. Phys. Oceanogr.,* **27**, 2087-2099.

Donelan, M.A., J. Hamilton, and W.H. Hui, 1985: Directional spectra of wind generated waves. *Phil. Trans. R. Soc. London, Ser. A*, **315**, 509-562.

Drennan, W.M., H.C. Graber, and M.A. Donelan, 1999: Evidence for the effects of swell and unsteady winds on marine wind stress. *J. Phys. Oceanogr.,* **29,** 1853-1864.

Elfouhaily, T., B. Chapron, K. Katsaros, and D. Vandemark, 1997: A Unified directional spectrum for long and short wind-driven waves. *J. Geophys. Res., 107*, **15**, 781-15,796.

Guo-Larsen, X., V.K. Makin, and A.S. Smedman, 2003: Impact of waves on the sea drag: measurements in the Baltic Sea and a model interpretation. *The Glob. Atm. Oc. System.*, **9**, 97-120.

Hatori, M., M. Tokuda, and Y. Toba, 1981: Experimental study on strong interaction between regular waves and wind waves. *J. Oceanogr. Soc. Japan*, **37**, 111-119.

Kahma, K.K., and C.J. Calkoen, 1992: Reconciling discrepancies in the observed growth of wind-generated waves. *J. Phys. Oceanogr.,* **22,** 1389-1405.

Kharif, C., and A. Ramamonjiarisoa, 1988: Deep water gravity wave instabilities at large steepness. *Phys. Fluid*, **31**, 1286-1288.

Kudryavtsev, V.N., and V.K. Makin, 2001: The impact of air-flow separation on the drag of the sea surface. *Boundary-Layer Meteorol.*, **98**, 155-171.

Kudryavtsev, V.N., and V.K. Makin, 2004: Impact of swell on marine atmospheric boundary layer. *J. Phys. Oceanogr.*, **34**, 934-949.

Kudryavtsev, V.N., V.K. Makin, and B. Chapron, 1999: Coupled sea surface-atmosphere model 2. Spectrum of short wind waves. *J. Geophys. Res.*, **104**, 7625-7639.

Longuet-Higgins, M.S., 1957: The statistical analysis of a random moving surface. *Phil. Trans. R. Soc. London, Ser. A*, **249**, 321-387.

Maat, N., and V.K. Makin, 1992: Air-flow above breaking waves. *Boundary-Layer Meteorol.*, **60**, 77-93.

Makin, V.K., and V.N. Kudryavtsev, 1999: Coupled sea surface- atmosphere model 1. Wind over waves coupling. *J. Geophys. Res.*, **104**, 7613-7623.

Makin, V.K., and V.N. Kudryavtsev, 2002: Impact of dominant waves on sea drag. *Boundary-Layer Meteorol.*, **103**, 83-99 .

Makin, V.K., and V.N. Kudryavtsev, 2003: Wind - over - waves coupling. In *Wind Over Waves II: Forecasting and Fundamentals of Application*, pp. 46-56, editors: S.G. Sajjadi and J.C.R. Hunt, Horwood Publishing Limited, Chichester, England.

Makin V.K., V.N. Kudryavtsev, and C. Mastenbroek, 1995: Drag of the sea surface. *Boundary-Layer Meteorol.*, **79**, 159-182.

Meirink, J.F., V.N. Kudryavtsev, and V.K. Makin, 2003: Note on the growth rate of water waves propagating at an arbitrary angle to the wind. *Boundary-Layer Meteorol.*, **106**, 171-183.

Mitsuyasu, H., 1966: Interactions between water waves and wind (I). *Rep. Inst. Appl. Mech. Kyushu Univ.*, **14**, 67-88.

Peirson, W.L., H. Branger, J.P. Giovanangeli, and M.L. Banner, 2004: The response of wind drag to underlying swell slope. *WRL Research Report No. 223*, The University of New South Wales, Water Research Laboratory, Manly Vale N.S.W., Australia, 23 p.

Phillips, O.M., 1985: Spectral and statistical properties of the equilibrium range in wind generated gravity waves. *J. Fluid Mech.*, **156**, 505-531.

Phillips, O.M., and M.L. Banner, 1974: Wave breaking in the presence of wind drift and swell. *J. Fluid Mech.*, **66**, 625-640.

Song, J.B., and M.L. Banner, 2002: On determining the onset and strength of breaking for deep water waves. Part I: Unforced irrotational wave groups. *J. Phys.Oceanogr.,* **32**, 2541-2558.

Srokosz, M.A., 1986: On the probability of wave breaking in deep water. *J. Phys. Oceanogr.*, **16**, 382-385.

Stewart, R.W., 1974: The air-sea momentum exchange. *Boundary-Layer Meteorol.*, **6**, 151-167.

Xu, D., P.A. Hwang, and J. Wu,1986: Breaking of wind-generated waves. *J. Phys.Oceanogr.,* **16**, 2172-2178.

Yelland, M., and P. Taylor, 1996: Wind stress measurements from the open ocean. *J. Phys. Ocean.*, **26**, 541-558.

Yermakov, S.A., K.D. Ruvinskiy, S.G. Salashin, and G.I. Freydman, 1986: Experimental investigation of the generation of capillary-gravity ripples by strongly non-linear waves on the surface of a deep fluid. *Izv. Atmos. Ocean Phys.*, **22**, 835-842.

V. K. Makin, Royal Netherlands Meteorological Institute, P.O. Box 201, 3730 AE De Bilt, Netherlands. (e-mail: makin@knmi.nl)

H. Branger, Institut de Recherche sur les Phénomènes Hors Equilibre, CNRS, Université de Provence, Aix-Marseille Université, 163, av. de Luminy, case 903, 13009 Marseille, France. (e-mail: branger@irphe.univ-mrs.fr)

W. L. Peirson, Water Research Laboratory, School of Civil and Environmental Engineering, The University of New South Wales, King st., Manly Vale NSW 2093, Australia. (e-mail: W.Peirson@unsw.edu.au)

J. P. Giovanangeli, Institut de Recherche sur les Phénomènes Hors Equilibre, CNRS, Université de Provence, Aix-Marseille Université, 163, av. de Luminy, case 903, 13009 Marseille, France. (e-mail: giovanangeli@irphe.univ-mrs.fr)

Received February 0, 2005

To appear in the *Journal of Physical Oceanography*, 2007

CAPTIONS TO FIGURES

Figure 1. Observed ratio of the stress supported by paddle plus wind-generated waves τ_{pww} to the stress supported by pure wind-generated waves τ_{ww} as a function of the paddle wave steepness AK.

Figure 2. Measured wave spectra for runs G000010A (pure wind-generated waves, U_{ref}=10 ms^{-1})- solid line, and G143010A (wind-generated and paddle waves, U_{ref}=10 ms^{-1}, AK=0.13)- dashed line. Modelled spectra for the same runs are shown by dashed-dotted lines.

Figure 3. Damping parameter γ_d specified by Equation (21) as a function of the paddle wave steepness AK.

Figure 4. Measured against modelled stress. Bars correspond to the overall error of 20% in measured stress. Thick solid line indicates the regression line.

Figure 5. Modelled ratio of the stress supported by paddle plus wind-generated waves τ_{pww} to the stress supported by pure wind-generated waves τ_{ww} as a function of the paddle wave steepness AK.

Figure 6. Stress components according to (19) for G- and H-series as a function of the paddle wave steepness AK. See legend for notations. Notice, that the wave-induced stress τ_w^f is split into $\tau_{w_d}^f$ - wave-induced stress supported by dominant wind-generated waves, and $\tau_{w_{eq}}^f$ - wave-induced stress supported by waves in the equilibrium range.

Figure 7. Fractional contribution of the stress components in (19) to the total stress, for runs G000010A (pure wind-generated waves, U_{ref}=10 ms^{-1}), G141010A (wind-generated and paddle waves, U_{ref}=10 ms^{-1}, AK=0.12), and G149010B (wind-generated and paddle waves, U_{ref}=10 ms^{-1}, AK=0.27).

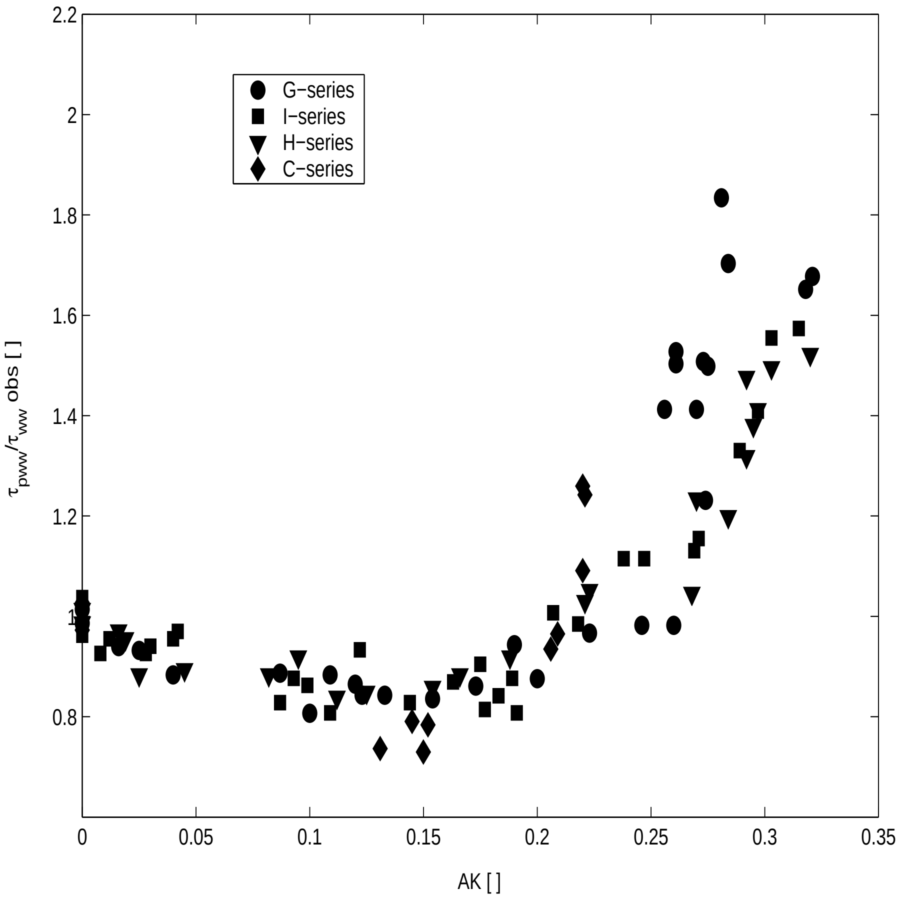

Figure 1: Observed ratio of the stress supported by paddle plus wind waves τ_{pww} to the stress supported by pure wind waves τ_{ww} as a function of the paddle wave steepness AK.

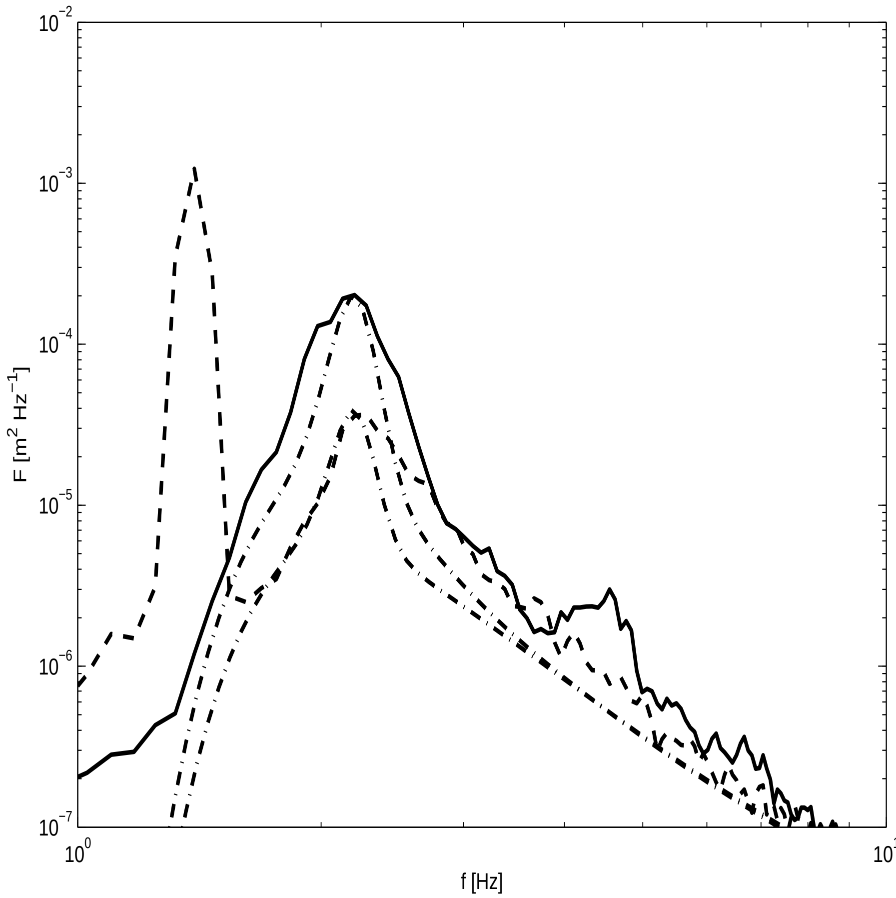

Figure 2: Wave spectra for runs G000010A (pure wind waves, U_{ref}=10 ms^{-1})-solid line, and G143010A (wind and paddle waves, U_{ref}=10 ms^{-1}, AK=0.13)-dashed line. Modelled spectra for the same runs are shown by dashed-dotted lines.

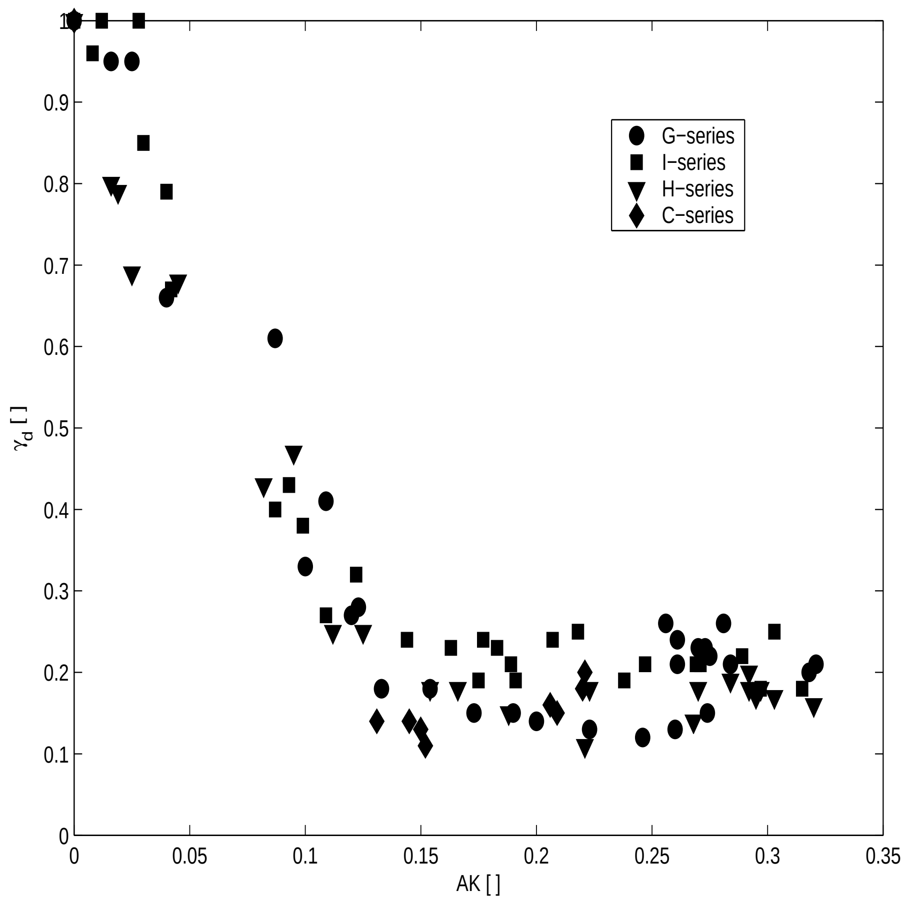

Figure 3: Damping parameter γ_d specified by (21) as a function of the paddle wave steepness AK.

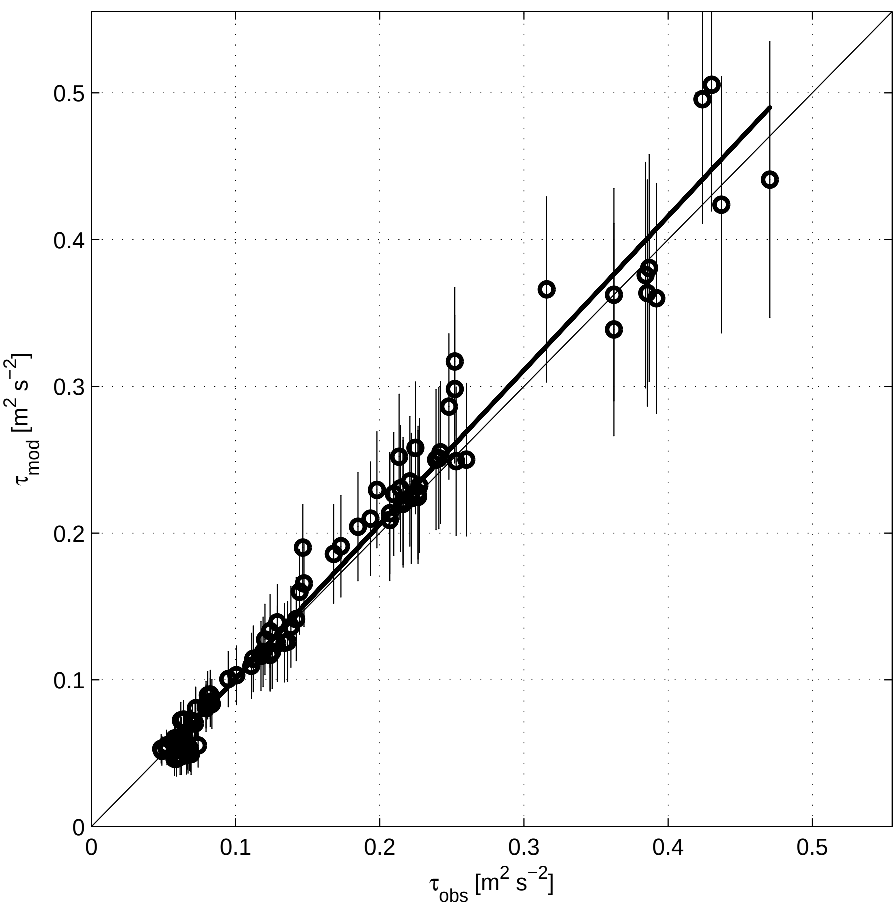

Figure 4: Measured against modelled stress. Bars correspond to the overall error of 20% in measured stress. Thick solid line indicates the regression line.

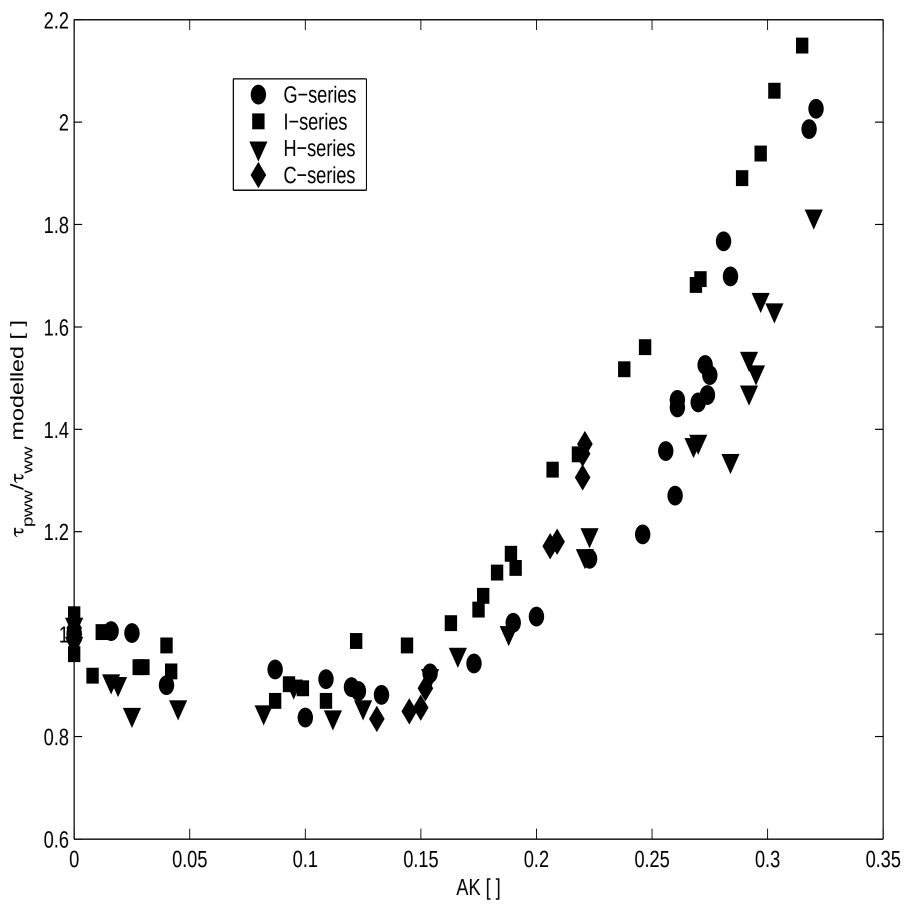

Figure 5: Modelled ratio of the stress supported by paddle plus wind waves τ_{pww} to the stress supported by pure wind waves τ_{ww} as a function of the paddle wave steepness AK.

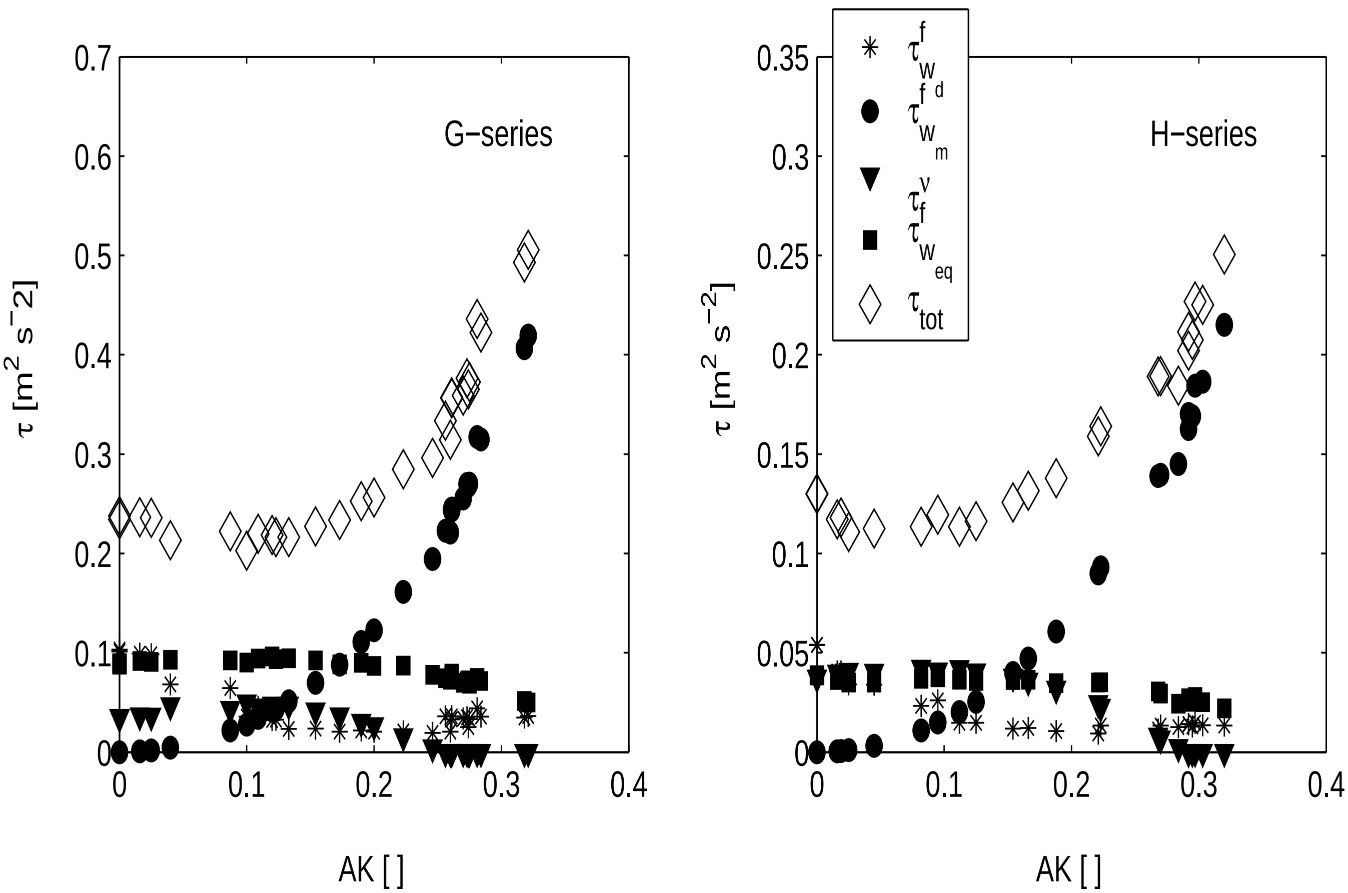

Figure 6: Stress components according to (19) for G- and H-series as a function of the paddle wave steepness AK. See legend for notations. Notice, that the wave-induced stress τ_w^f is split into $\tau_{w_d}^f$ - wave-induced stress supported by dominant wind waves, and $\tau_{w_{eq}}^f$ - wave-induced stress supported by waves in the equilibrium range.

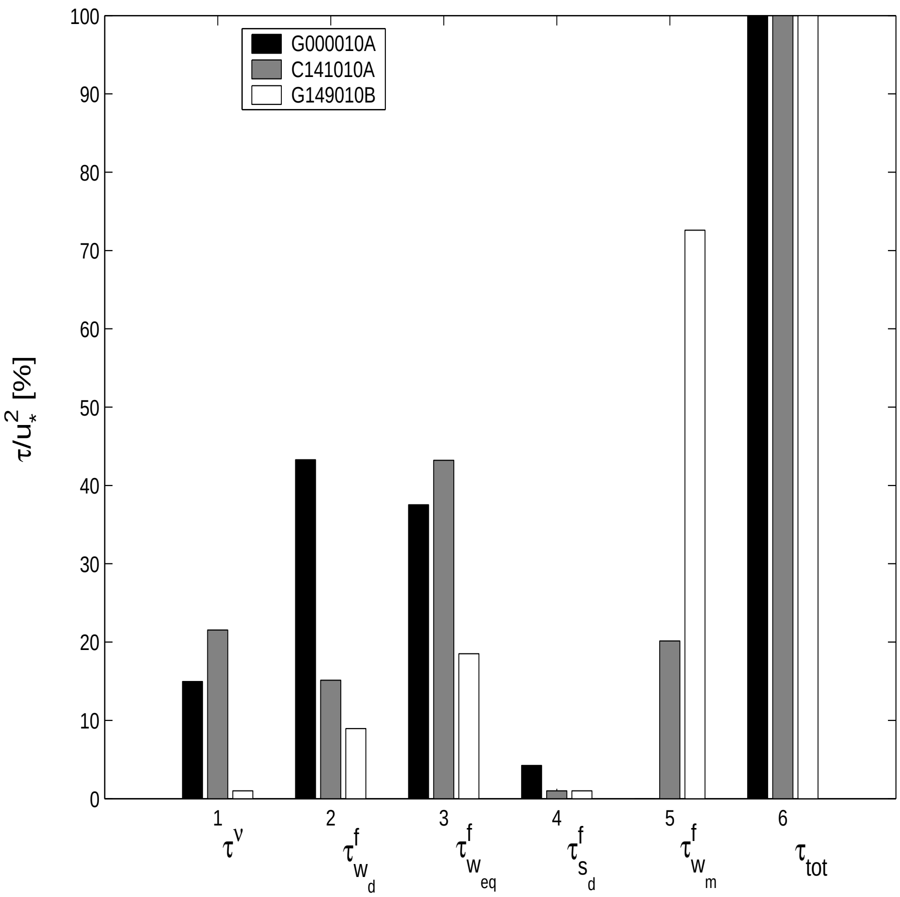

Figure 7: Fractional contribution of the stress components in (19) to the total stress, for runs G000010A (pure wind waves, U_{ref}=10 ms^{-1}), G141010A (wind and paddle waves, U_{ref}=10 ms^{-1}, AK=0.12), and G149010B (wind and paddle waves, U_{ref}=10 ms^{-1}, AK=0.27).

Table 1: Summary results for G-series with the reference speed $U_{ref} = 10\text{ms}^{-1}$, the frequency of the paddle wave $f_m = 1.4$ Hz, and the peak frequency of the wind waves $f_p = 2.18$ Hz. AK is the paddle wave steepness, U_{10} is the reference wind speed at 10 m height, $u_{*_{obs}}$ is the measured friction velocity, $u_{*_{mod}}$ is the modelled friction velocity, and γ_d is the damping parameter according to (21).

N	run G-series	AK []	U_{10} ms^{-1}	$u_{*_{obs}}$ ms^{-1}	$u_{*_{mod}}$ ms^{-1}	γ_d []
1	G000010A	0	12.97	0.503	0.499	1
2	G000010B	0	13.04	0.510	0.500	1
3	G140510A	0.025	13.06	0.489	0.500	0.95
4	G140510B	0.016	13.09	0.491	0.501	0.95
5	G140810A	0.087	13.02	0.477	0.482	0.61
6	G140810B	0.040	12.97	0.476	0.474	0.66
7	G141010A	0.123	13.03	0.465	0.471	0.28
8	G141010B	0.109	13.06	0.476	0.477	0.41
9	G142010A	0.120	13.12	0.471	0.473	0.27
10	G142010B	0.100	12.84	0.455	0.457	0.33
11	G143010A	0.133	13.06	0.465	0.469	0.18
12	G143010B	0.154	13.08	0.463	0.480	0.18
13	G144010A	0.173	13.02	0.470	0.485	0.15
14	G144010B	0.190	13.21	0.492	0.505	0.15
15	G144510A	0.223	13.41	0.498	0.535	0.13
16	G144510B	0.200	13.16	0.474	0.508	0.14
17	G144810A	0.260	13.30	0.502	0.563	0.13
18	G144810B	0.246	13.27	0.502	0.546	0.12
19	G145010A	0.274	13.74	0.562	0.605	0.15
20	G146010A	0.318	14.27	0.651	0.704	0.20
21	G146010B	0.321	14.33	0.656	0.711	0.21
22	G147010A	0.284	14.23	0.661	0.651	0.21
23	G147010B	0.281	14.42	0.686	0.664	0.26
24	G148010A	0.270	13.62	0.602	0.602	0.23
25	G148010B	0.273	13.81	0.622	0.617	0.23
26	G149010A	0.261	13.84	0.626	0.600	0.21
27	G149010B	0.275	13.72	0.620	0.613	0.22
28	G149910A	0.261	13.78	0.621	0.603	0.24
29	G149910B	0.256	13.51	0.602	0.582	0.26

Table 2: Summary results for H-series with the reference speed $U_{ref} = 8\text{ms}^{-1}$, the frequency of the paddle wave $f_m = 1.6$ Hz, and the peak frequency of the wind waves $f_p = 2.38$ Hz.

N	run	AK	U_{10}	$u_{*_{obs}}$	$u_{*_{mod}}$	γ_d
	H-series	[]	ms^{-1}	ms^{-1}	ms^{-1}	[]
1	H000080A	0	10.39	0.372	0.369	1
2	H000080B	0	10.40	0.377	0.376	1
3	H160580A	0.019	10.22	0.366	0.354	0.79
4	H160580B	0.016	10.18	0.369	0.355	0.80
5	H160880A	0.025	10.07	0.352	0.342	0.69
6	H160880B	0.045	10.09	0.354	0.345	068
7	H161080A	0.082	10.23	0.352	0.343	0.43
8	H161080B	0.095	10.31	0.359	0.353	0.47
9	H162080A	0.125	10.20	0.345	0.345	0.25
10	H162080B	0.112	10.22	0.343	0.341	0.25
11	H163080A	0.154	10.30	0.347	0.357	0.18
12	H163080B	0.166	10.35	0.352	0.365	0.18
13	H164080A	0.221	10.53	0.380	0.400	0.11
14	H164080B	0.188	10.31	0.359	0.373	0.15
15	H165080A	0.223	10.58	0.384	0.407	0.18
16	H165080B	0.268	10.61	0.383	0.436	0.14
17	H166080A	0.297	10.88	0.445	0.479	0.18
18	H166080B	0.270	10.55	0.416	0.437	0.18
19	H167080A	0.303	10.72	0.458	0.476	0.17
20	H167080B	0.320	10.83	0.462	0.502	0.16
21	H168080A	0.292	10.68	0.455	0.462	0.18
22	H168080B	0.295	10.54	0.440	0.458	0.17
23	H169980A	0.284	10.21	0.410	0.431	0.19
24	H169980B	0.292	10.46	0.430	0.452	0.20

Table 3: Summary results for C-series with the reference speed $U_{ref} = 6\text{ms}^{-1}$, the frequency of the paddle wave $f_m = 2$ Hz, and the peak frequency of the wind waves $f_p = 2.68$ Hz.

N	run	AK	U_{10}	$u_{*_{obs}}$	$u_{*_{mod}}$	γ_d
	C-series	[]	ms^{-1}	ms^{-1}	ms^{-1}	[]
1	C000060A	0	7.68	0.261	0.247	1
2	C000060B	0	7.61	0.254	0.250	1
3	C202060A	0.150	7.26	0.220	0.230	0.13
4	C202060B	0.145	7.26	0.229	0.229	0.14
5	C203060A	0.152	7.37	0.228	0.235	0.11
6	C203060B	0.131	7.34	0.221	0.227	0.14
7	C204060A	0.209	7.64	0.253	0.270	0.15
9	C204560A	0.206	7.64	0.249	0.269	0.16
10	C204560B	0.220	7.82	0.269	0.284	0.18
11	C205060B	0.220	7.96	0.289	0.289	0.18
12	C205060C	0.221	7.98	0.287	0.291	0.20

Table 4: Summary results for I-series with the reference speed $U_{ref} = 6\text{ms}^{-1}$, the frequency of the paddle wave $f_m = 1.4$ Hz, and the peak frequency of the wind waves $f_p = 2.64$ Hz.

N	run I-series	AK []	U_{10} ms^{-1}	$u_{*_{obs}}$ ms^{-1}	$u_{*_{mod}}$ ms^{-1}	γ_d []
1	I000060A	0	7.08	0.262	0.226	1
2	I000060B	0	7.27	0.272	0.235	1
3	I140560A	0.008	7.03	0.257	0.221	0.96
4	I140560B	0.012	7.06	0.261	0.231	1
5	I140860A	0.028	7.05	0.257	0.223	1
6	I140860B	0.030	7.17	0.259	0.223	0.85
7	I141060A	0.042	7.19	0.263	0.222	0.67
8	I141060B	0.040	7.21	0.261	0.228	0.79
9	I142060A	0.087	7.17	0.243	0.215	0.40
10	I142060B	0.093	7.25	0.250	0.219	0.43
11	I143060A	0.099	7.22	0.248	0.218	0.38
12	I143060B	0.109	7.08	0.240	0.215	0.27
13	I144060A	0.122	7.36	0.258	0.229	0.32
14	I144060B	0.144	7.19	0.243	0.228	0.24
15	I144560A	0.175	7.12	0.254	0.236	0.19
16	I144560B	0.163	7.13	0.249	0.233	0.23
17	I144860A	0.189	7.24	0.250	0.248	0.21
18	I144860B	0.191	7.13	0.240	0.245	0.19
19	I145060A	0.183	7.17	0.245	0.244	0.23
20	I145060B	0.177	7.13	0.241	0.239	0.24
21	I146060A	0.207	7.44	0.268	0.265	0.24
22	I146060B	0.218	7.39	0.265	0.268	0.25
23	I147060A	0.238	7.53	0.282	0.284	0.19
24	I147060B	0.247	7.52	0.282	0.288	0.21
25	I148060A	0.271	7.50	0.287	0.300	0.21
26	I148060B	0.269	7.48	0.284	0.299	0.21
27	I149060A	0.289	7.64	0.308	0.317	0.22
28	I149060B	0.297	7.66	0.317	0.321	0.18
29	I149960A	0.315	7.79	0.335	0.338	0.18
30	I149960B	0.303	7.77	0.333	0.331	0.25